ISSN (Print) 1226-1750
ISSN (Online) 2233-6656
Journal of Magnetics 25(1), 70-77 (2020) https://doi.org/10.4283/JMAG.2020.25.1.070

Design and Output Characteristic Analysis of 3-D Micron-scale Actuator

Yafang Li[1,2], Bowen Wang[1,2], and Wenmei Huang[1,2]*

[1]*State Key Laboratory of Reliability and Intelligence of Electrical Equipment, Hebei University of Technology, Tianjin, China*
[2]*Key Laboratory of Electromagnetic Field and Electrical Apparatus Reliability of Hebei Province, School of Electrical Engineering, Hebei University of Technology, Tianjin, China*

(Received 28 March 2019, Received in final form 27 December 2019, Accepted 27 December 2019)

A new type of 3-D micron-scale actuator is designed, which is mainly composed of four Galfenol rods, drive coils, base, magnetic yoke and output head. According to magnetostrictive model and structural dynamic model, the output characteristics of the actuator have been analyzed. The 3-D moving trail of the output head is controlled by the drive coils of the four rods. The actuator prototype is fabricated and experimental investigated. Good agreement is observed between the simulation and experimental results. The maximum output displacements of the X, Y and Z direction are 46 μm, 46 μm and 8.2 μm. Furthermore, when a pair of opposing rods works, the actuator has two modes of vibration under 1000 Hz. The resonant frequencies of the actuator are 522 Hz in Y direction and X direction. The results have proved that the actuator can realize varied 3-D displacement according to actual demands, and can be used in 3-D micron-scale field, such as surface mold polishing.

Keywords : galfenol, actuator, 3-D micron-scale and output characteristic

1. Introduction

The trend toward miniaturization of industrial devices demands innovation in materials and fabrication technology. The low light level lens which is in the optical devices such as digital camera and blue light player are made by precision polishing. The process becomes more difficult as the mold size decreases and the required accuracy increases [1]. In the conventional polishing method, a rotating soft polishing tool has been used to polish the workpiece surface. In this method, the mechanism is complex and the polishing force is difficult to control [2]. As the shape of the workpiece and the radius of curvature become smaller, typically less than 3 mm in diameter, it becomes difficult to apply this polishing method. Therefore, it is necessary to design a micro actuator which can achieve micro-scale precision polishing with smart materials.

Iron-Gallium alloy (Galfenol) is a kind of magnetostrictive material. It has magnetostriction (~350 ppm) under low saturation field (~100 Oe), exhibits high tensile strength (~500 MPa) and very low hysteresis [3]. Moreover, it has machinability, corrosion resistance and antifatigue properties over time [4, 5]. All these factors demonstrate that Galfenol is suitable for micro-scale actuation and sensing applications [6, 7]. For the actuators with a single magnetostrictive rod, the output characteristics in one dimension were studied. Xue Guangming designed a magnetostrictive actuator which can produce axial output displacement [8]. Xu Yan developed a bending vibration of the composite cantilever beam with magnetostrictive layer. The radial dynamic characteristics were analyzed [9]. Then the actuators with two magnetostrictive rods were studied. Wang Zhenyu presented a new type of a dual magnetostrictive material rods actuator. It can achieve continuous displacement of the actuator [10]. Li Yafang designed and manufactured a double-Galfenol-rods magnetostrictive transducer. The device can simultaneously generate output displacement in axial and radial direction [11]. A two-dimensional constitutive model based on micromechanical domain rotation events was presented to demonstrate the nonlinear actuator behavior of magnetostrictive materials, in particular, Galfenol [12]. Further, for the actuators with four magnetostrictive rods, Toshiyuki Ueno studied a miniature three dimension (3-D) spherical motor using Galfenol. This motor consists of

*Corresponding author: Tel: +8618526455969
Fax: +8618526455969, e-mail: huzwm@hebut.edu.cn

four rods of Galfenol. The maximum displacement exerted on the motor was 2.2 μm [13]. Guo Jiang proposed a magnetostrictive vibrating actuator. The actuator vibrated in a lateral motion at frequency of 9.2 kHz with amplitude of 30 μm. The polishing force was controllable within a range of 2-200 mN [14]. For special shape actuators, Tadashi Kosawada developed an actuator with Z-shaped steric structure. It can excite 3-D vibrations in its micro-probe with total amplitude of displacement up to 30 μm in each X, Y and Z direction [15]. Nevertheless, few reports on the theoretical and experimental researches of magnetostrictive actuator which can achieve micron-scale output displacement and large output force at low frequency have been found. In this paper, a novel 3-D micron-scale actuator is design. The output characteristics are studied by theoretical and experimental methods. It can be used in 3-D micron-scale field, such as surface mold polishing.

2. Structural Design and Output Characteristic Analysis of Actuator

2.1. Structural design of actuator

The designed 3-D micron-scale actuator depicted in Fig. 1 consists of four Galfenol rods, four drive coils, base, magnetic yoke and output head. A Galfenol cube raw material is machined by wire-electrode cutting, and the four perfectly symmetrical Galfenol rods with square cross section are obtained. The designed dimensions of the Galfenol rods are 4 mm×4 mm×34 mm. To reduce the effect of eddy current loss, the Galfenol rods are machined into 1 mm slices and glued together by epoxy resin. The applied magnetic field is 5 kA/m. This translates to number of each coil turns as 300, resistance of 1.7 Ω, a bias current of 0.3 A and exciting current of 0.2 A. Industrial No.45 steel is used to manufacture magnetic

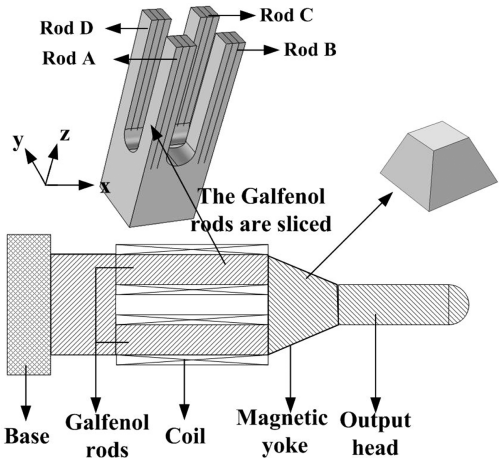

Fig. 1. Structure diagram of actuator.

yoke which presents high magnetic conductivity, toughness, and machinability. The magnetic yoke is designed as a hexahedral structure, as shown in Fig. 1. It ensures the closure of the magnetic circuit, and the volume of the magnetic yoke is reduced, so that the output force can effectively drive the output head to produce mechanical vibration. The base is also made of industrial No. 45 steel. It is fixed thus the actuator outputs mechanical vibrations from the output head. The output head is processed by high hardness stainless steel.

The 3-D moving trail of the output head is controlled by the drive coils of four rods (anti-clockwise numbers labeled as A, B, C and D). When the four rods are applied with same direction bias and exciting current, the rods are extended or shortened simultaneously, so that the actuator can generate axial output displacement. When the same direction bias current and an exciting current of 180° phase difference passes on the a pair of opposing coils, e.g., A and C, the movement state of the two rods is opposite. The output head can generate 3-D displace-

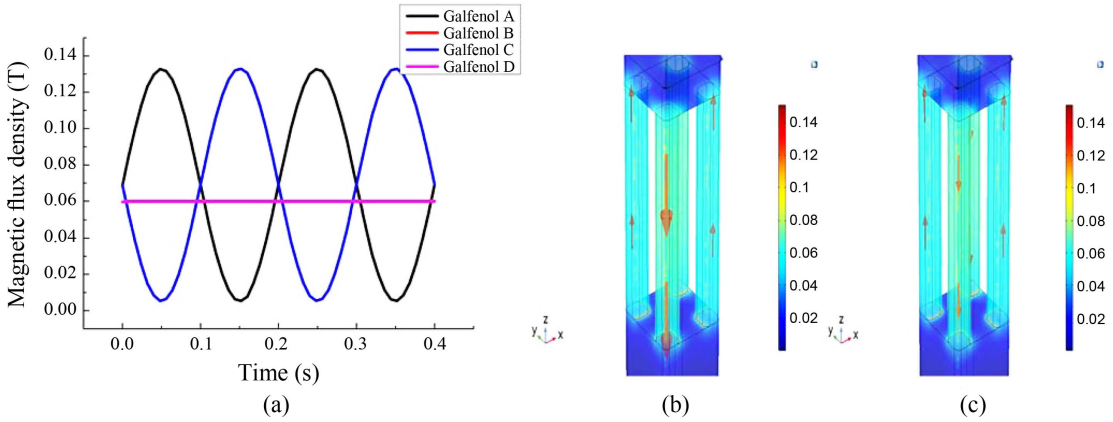

Fig. 2. (Color online) Magnetic flux density (a) magnetic flux density of the four rods; (b) magnetic flux density distribution at 0.056 s; (c) magnetic flux density distribution at 0.104 s.

ments. The X direction, Y direction and Z direction are determined as shown in Fig. 1. The normal vector direction of the plane B and C rods located is X direction. The axial direction is Z direction.

Figure 2 shows magnetic flux density at the center of the four rods when a pair of opposing rods (the rod A and rod C) work. The phase difference of the magnetic flux density of rod A and rod C is 180°. The peak values of the magnetic flux density of rod A and rod C are 0.13 T. It is larger than that of rod B and rod D which are almost stable at 0.06 T. The results show that the magnetic circuit is formed between the four rods. What's more, there is very little leakage flux. Compared with the traditional magnetostrictive devices, the closed magnetic circuit forming between the four rods, which makes the actuator has good heat dissipation and simplifies the structure of actuator. Therefore, the designed actuator has obvious advantages.

Figure 2b and Fig. 2c show the magnetic flux density distributions of actuator at 0.056 s (1/4 period) and 0.104 s (1/2 period). The red arrow is a vector whose size and direction represent the magnitude and direction of the flux density. As a result, the distribution and flow direction of the magnetic flux are shown more intuitively.

2.2. Output characteristic analysis of actuator

Based on the magnetostrictive effect [16], the Galfenol rods change their deformation when subjected to an external magnetic field and stress. They are used as the vibration sources to drive the output head movement. The output characteristic of the actuator is controlled by the four Galfenol rods. Because the actuator is symmetrical structure, firstly, the output characteristics of the actuator under single Galfenol rod motion are analyzed. In the movement of the actuator, based on the principle of structural mechanics, solid mechanics and d'Alembert principle, the displacement of the bottom of the Galfenol rod is 0 mm. The top of the Galfenol rod has the same displacement y, velocity $\dot{y}$ and acceleration $\ddot{y}$ as output head of actuator. In addition, the stress generated by Galfenol rod, F_r, and the stress acting on the rod by the output head, F_l, agree with Newton's third law. In this way, the dynamic motion of the actuator is simplified as equivalent single-degree-of-freedom system, as shown in Fig. 3. The Galfenol rod and the output head are simplified to equivalent spring and mass, respectively. Where, m_r is the mass of Galfenol rod. K_r is the stiffness coefficient of Galfenol rod. m_l is the mass of output head. K_l is the stiffness coefficient of output head.

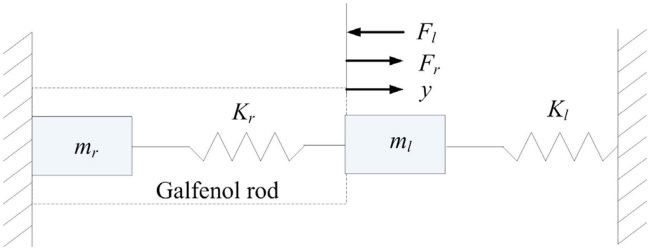

Fig. 3. (Color online) Equivalent mechanical system of actuator.

For a Galfenol rod, the vibration system of single-degree-of-freedom, as shown in

$$m_r\ddot{y} + K_r y = F_l(t) \tag{1}$$

Where, $F_l(t) = F_m \sin \eta t$. F_m is the amplitude of stress. When bias magnetic field is applied to the rod, the initial conditions of the Galfenol rod is

$$\begin{aligned} y(0) &= \frac{\Delta l}{2} \\ \dot{y}(0) &= 0 \end{aligned} \tag{2}$$

Where Δl is the elongation in the longitudinal direction of the rod. According to the initial conditions, differential Eq. (1) is solved. The displacement of Galfenol rod can be computed, as shown in

$$y = -\frac{F_m \eta}{m_r \omega(\omega^2 - \eta^2)} \sin \omega t + \frac{\Delta l}{2} \cos \omega t + \frac{F_m}{m_r(\omega^2 - \eta^2)} \sin \eta t \tag{3}$$

Where, $\omega = \sqrt{K/m}$. The parameters to be identified are $F_l(t)$ and Δl. Owning to the stress generated by a Galfenol rod $F_r(t)$ and $F_l(t)$ agree with Newton's third law, $F_l(t) = -F_r(t)$. The stress generated by a Galfenol rod is given by

$$F_r = EA\lambda \tag{4}$$

E is young's modulus. A is area of Galfenol rod [17]. λ is magnetostriction of Galfenol.

$$\begin{aligned} \lambda(\sigma, H) = \iint ((3/2)\lambda_{100}(\alpha_1^2\beta_{1R}^2 + \alpha_2^2\beta_{2R}^2 + \alpha_3^2\beta_{3R}^2 - 1/3) \\ + 3\lambda_{111}(\alpha_1\alpha_2\beta_{1R}\beta_{2R} + \alpha_2\alpha_3\beta_{2R}\beta_{3R} + \alpha_1\alpha_3\beta_{1R}\beta_{3R})) \\ \cdot f(\theta, \xi) \sin\theta d\theta d\xi \end{aligned} \tag{5}$$

Where the direction cosine (α_1, α_2, α_3) and (β_{1R}, β_{2R}, β_{3R}) are the respectively determined by magnetization and measuring direction along magnetic crystal axis. The λ_{100} and λ_{111} are magnetostrictive constants in $\langle 100 \rangle$ and $\langle 111 \rangle$ direction. The $f(\theta, \xi)$ is the distribution probability function. It is the probability of magnetic crystal magnetization along the direction of (θ, ξ) [18]. λ_s is the saturation magnetostriction of Galfenol. It is determined by Eq. (5). When the rod works at the optimum working conditions, the governing equation is $I = 0.3 + 0.2\sin(2\pi ft)$ A. The stress of rod can be calculated by

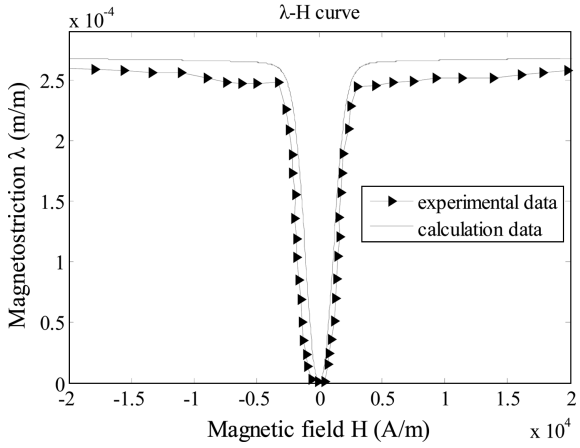

Fig. 4. Magnetic field dependence of magnetostriction for Galfenol.

$$F_r(t) = EA(\lambda_s / 2 + (\lambda_s / 2)\sin(\eta t)) \tag{6}$$

The elongation in the direction of the rod length is represented by

$$\Delta l = \lambda(\sigma, H) \cdot l \tag{7}$$

Where, l is the length of rod. When the Galfenol rod works at its optimum working conditions, the output characteristics are calculated using the following parameters: $\lambda_{100} = 2.12\times10^{-4}$, $\lambda_{111} = 1.3\times10^{-5}$, $l = 34$ mm, $E = 59$ GPa, $A = 1.6\times10^{-5}$, $K_r = 2.8\times10^{7}$ N/m, $m_r = 4.1$ g, $m_l = 5.1$g and $K_l = 1.6\times10^{9}$ N/m [18]. The magnetostrictive curves of the Galfenol are obtained by calculation and experiment, as shown in Fig. 4. The saturation magnetostriction λ_s is 270 ppm. By Eq. (1)-(7), the output displacement of the system under a Galfenol rod motion can be obtained. According to output head has the same displacement y, velocity $\dot{y}$ and acceleration $\ddot{y}$ as the top of the Galfenol rod, the output displacement of output head can be calculated.

Based on the design theory, when same direction bias current and an exciting current of 180° phase difference flows in a pair of opposing coils (A and C, B and D), the movement state of the two rods is opposite. Moreover, there is a φ phase difference between rod A and rod B, as shown in Eq. (8). So, the output head can generate 3-D output displacements. According to circuit, magnetic circuit and magnetostriction theory, the bias magnetic field and exciting magnetic field for rods are determined by

$$\begin{aligned} I_A &= I_0 + i\sin(2\pi ft) \\ I_B &= I_0 + i\sin(2\pi ft + \varphi) \\ I_C &= I_0 + i\sin(2\pi ft + \gamma) \\ I_D &= I_0 + i\sin(2\pi ft + \gamma + \varphi) \end{aligned} \tag{8}$$

Where, I_0 is the bias current, i is the amplitude of exciting current. Then the displacements of the rods are

$$\begin{aligned} y_A &= -\frac{F_A\eta}{m_r\omega(\omega^2-\eta^2)}\sin\omega t + \frac{\lambda_s\cdot l}{2}\cos\omega t + \frac{F_A}{m_r(\omega^2-\eta^2)}\sin\eta t \\ y_B &= -\frac{F_B\eta}{m_r\omega(\omega^2-\eta^2)}\cos\varphi\cdot\sin\omega t + \frac{\lambda_s\cdot l}{2}\cos\omega t + \frac{F_B}{m_r(\omega^2-\eta^2)}\sin(\eta t+\varphi) \\ y_C &= \frac{F_C\eta}{m_r\omega(\omega^2-\eta^2)}\cdot\sin\omega t + \frac{\lambda_s\cdot l}{2}\cos\omega t - \frac{F_C}{m_r(\omega^2-\eta^2)}\sin\eta t \\ y_D &= \frac{F_D\eta}{m_r\omega(\omega^2-\eta^2)}\cos\varphi\cdot\sin\omega t + \frac{\lambda_s\cdot l}{2}\cos\omega t - \frac{F_D}{m_r(\omega^2-\eta^2)}\sin(\eta t+\varphi) \end{aligned} \tag{9}$$

Finally, the displacement of output head is

$$\begin{aligned} y = &(-\frac{F_A\eta}{m_r\omega(\omega^2-\eta^2)} - \frac{F_B\eta}{m_r\omega(\omega^2-\eta^2)}\cos\varphi + \frac{F_C\eta}{m_r\omega(\omega^2-\eta^2)} \\ &+ \frac{F_D\eta}{m_r\omega(\omega^2-\eta^2)}\cos\varphi)\cdot\sin\omega t \\ &+ 2\lambda_s l\cdot\cos\omega t + (\frac{F_A}{m_r(\omega^2-\eta^2)} - \frac{F_C}{m_r(\omega^2-\eta^2)})\cdot\sin\eta t \\ &+ (\frac{F_B}{m_r(\omega^2-\eta^2)} - \frac{F_D}{m_r(\omega^2-\eta^2)})\cdot\sin(\eta t+\varphi) \end{aligned} \tag{10}$$

The output force of the actuator F_A and F_l are opposite and equal. $F_A = M_l\ddot{y} + K_l y$, the output force of the actuator is

$$\begin{aligned} F = &(-\frac{F_A\eta}{m_r\omega(\omega^2-\eta^2)} - \frac{F_B\eta}{m_r\omega(\omega^2-\eta^2)}\cos\varphi + \frac{F_C\eta}{m_r\omega(\omega^2-\eta^2)} \\ &+ \frac{F_D\eta}{m_r\omega(\omega^2-\eta^2)}\cos\varphi)\cdot(K_l - m_l\omega^2)\cdot\sin\omega t \\ &+ 2\lambda_s l\cdot(K_l - m_l\omega^2)\cdot\cos\omega t + (\frac{F_A}{m_r(\omega^2-\eta^2)} - \frac{F_C}{m_r(\omega^2-\eta^2)}) \\ &\cdot(K_l - m_l\omega^2)\cdot\sin\eta t \\ &+ (\frac{F_B}{m_r(\omega^2-\eta^2)} - \frac{F_D}{m_r(\omega^2-\eta^2)})\cdot(K_l - m_l\omega^2)\cdot\sin(\eta t+\varphi) \end{aligned} \tag{11}$$

According to Eq. (10) and Eq. (11), we can calculate the output characteristic of the actuator. In the designed actuator, the four rods are directly contact with the air and have good heat dissipation, so that the effects of the eddy current can be neglected at low frequencies (under 50 Hz). The model can provide important guidance for designing 3-D micron-scale actuator.

Figure 5 shows the calculated displacements of actuator at 1 Hz frequency. The trajectories of the output head in 2-D plane when the four rods work ($\gamma = 180°$ and $\varphi = 0°$, 45°, 90°, 135° and 180°) are analyzed. When φ is 0° and 180°, the moving trail of output head is in a straight line. The amplitudes can reach 23 μm, thus the maximum displacements of X direction and Y direction are 46 μm. When φ is 45° and 135°, the moving trail is a elliptic trajectory. The two semi-axis are 21 μm and 8 μm. When φ is 90°, the trail is a circular orbit with a radius of 15

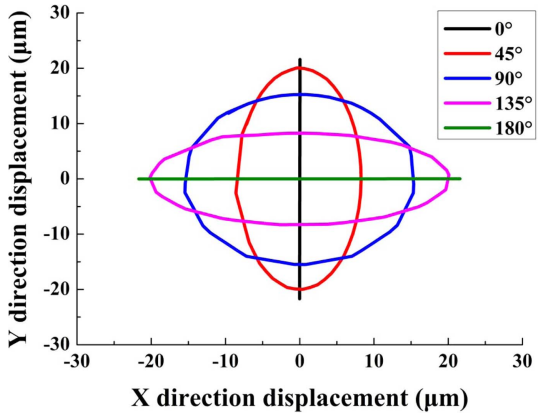

Fig. 5. (Color online) Moving trails of actuator ($\gamma = 180^{o}$ and $\varphi = 0°$, 45°, 90°, 135° and 180°).

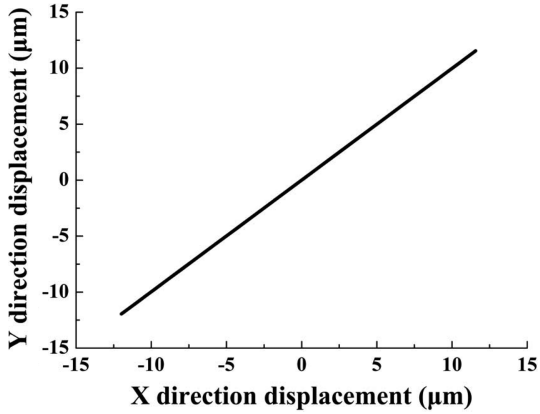

Fig. 6. Moving trails of actuator (the pair of rods A and C working).

μm. In addition, the range of Z direction displacement is 0 μm-4.6 μm.

The case in which the pair of A and C rods work is shown in Fig. 6. The output head is also vibrating in the diagonal direction of the 2-D plane. The maximum displacements of X direction and Y direction can reach 25 μm. However, the maximum displacement of Z direction can only reach 4 μm. Moreover, when four rods work at ($\gamma = 0^{o}$, $\varphi = 0^{o}$), the displacements of X direction and Y direction are basically 0 μm. It is vibrating in the Z direction, which can reach 8.2 μm. So, we can conclude that the 3-D moving trail of the actuator can be controlled by the four drive coils. The results show that the maximum displacements of X direction and Y direction realize at $\gamma = 180^{o}$ and $\varphi = 0°$ or 180°. What's more, the maximum displacements of Z direction realize at $\gamma = 0^{o}$, $\varphi = 0^{o}$.

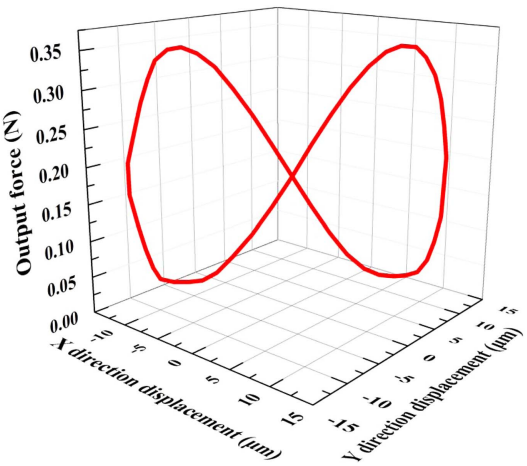

Fig. 7. (Color online) Output force of the actuator when the pair rods of A and C work.

Figure 7 shows the calculated output force of the actuator when a pair of opposing rods (the rod A and rod C) work. The force varies periodically with the vibration of the output head. In Fig. 7, the data of the X axis and the Y axis represent the actual vibration displacement of the output head. So, the output force at the vibration position of the output head is given in actual operation. The output force is controllable within a range of 0.04 N-0.34 N.

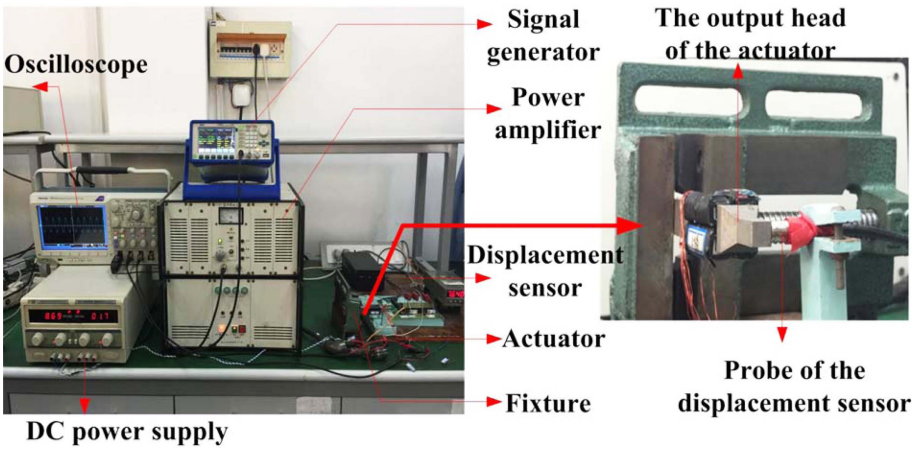

Fig. 8. (Color online) Experimental setup.

3. Experimental Results and Analysis

The output displacements of the actuator prototype are studied by experiment. The experimental system is shown in Fig. 8. It consists of DC power supply, signal generator, power amplifier, fixture, displacement sensor and oscilloscope. The DC power supply provides constant bias current for the actuator to reduce frequency-doubled effect. The signal generator and the power amplifier provide the dynamic driving current for the actuator. Under the bias and exciting magnetic fields, the displacement produced by output head is measured by capacitive non-contact displacement sensor, and the measuring device needs a plane. Thus the output head is processed into a cuboid to facilitate measurement. Finally, the signal is transmitted to the oscilloscope. The displacements of the output head in the X direction, the Y direction, and the Z direction are measured. The definition of the three directions is shown in Fig. 1.

Before the experiment, the Galfenol rod is demagnetized. The output head of the actuator and capacitive displacement sensor are located and adjusted. The capacitive displacement sensor is calibrated. Then, the optimum bias and exciting current are applied to the actuator. Finally, the experimental data are collected by displacement sensor. The output displacement of transducer is obtained by data processing. Since the capacitive displacement sensor can only measure one dimensional displacement, we measure the displacement in X direction and Y direction for each experiment.

The case in which the pair of rods A and C work is analyzed. Fig. 9 shows the moving trail of output head at 1 Hz driving frequency. The theoretically calculated value is compared with experiment and found that their changing tendencies are consistent. The maximum displacements

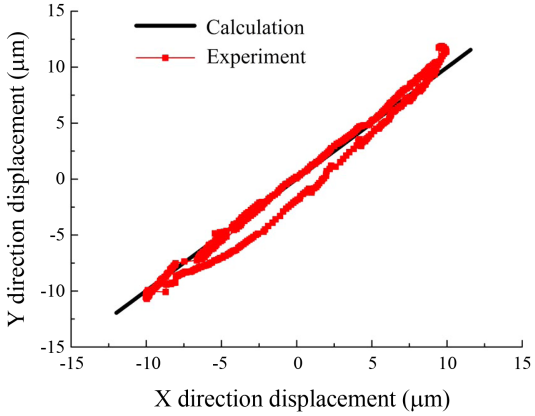

Fig. 9. (Color online) Moving trail of the actuator at 1 Hz frequency.

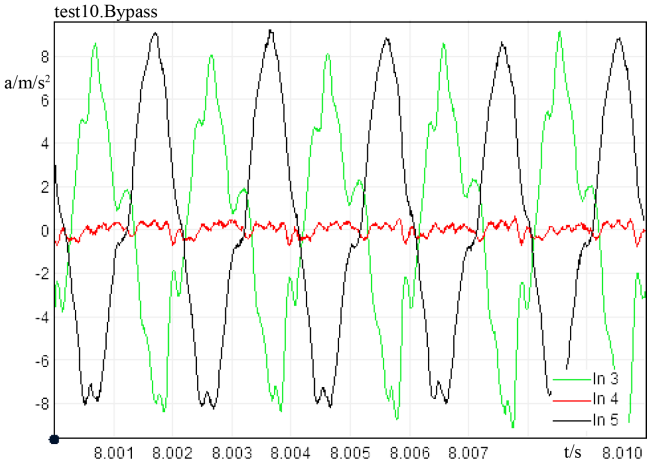

Fig. 10. (Color online) The acceleration of the actuator at 500 Hz frequency.

of X direction and Y direction of the calculation are 25 μm. By the experiment, the maximum displacements of X direction and Y direction are 22 μm and 23 μm, which are slightly smaller than calculated one. It is confirmed that the theoretical analysis coincide with experiment results. However, hysteresis loop exists in the experimental results. The reason is that there is an unavoidable energy loss in the actual operation of the actuator.

The output accelerations of the actuator are tested and analyzed. Based on the Newton's second law, the output force of the actuator can be calculated. The experimental method of the acceleration is the same as that of the

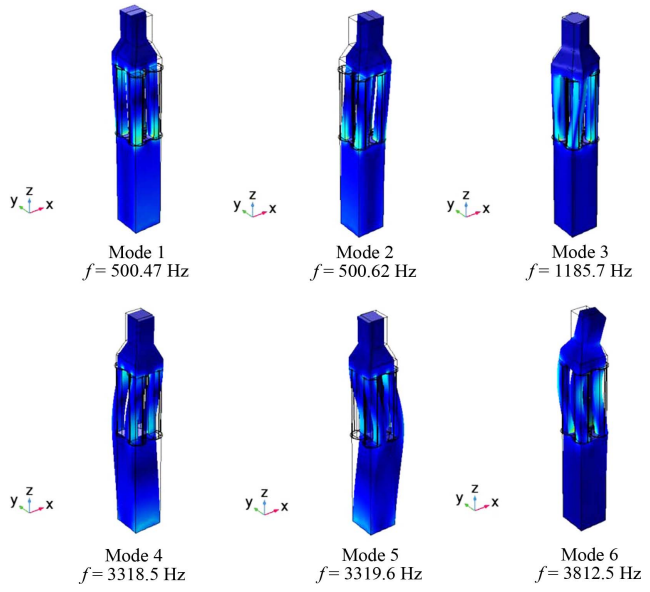

Fig. 11. (Color online) The first six modes and natural frequencies of the actuator (a) First order mode (b) Second order mode (c) Third order mode (d) Fourth order mode (e) Fifth order mode (f) Sixth order mode.

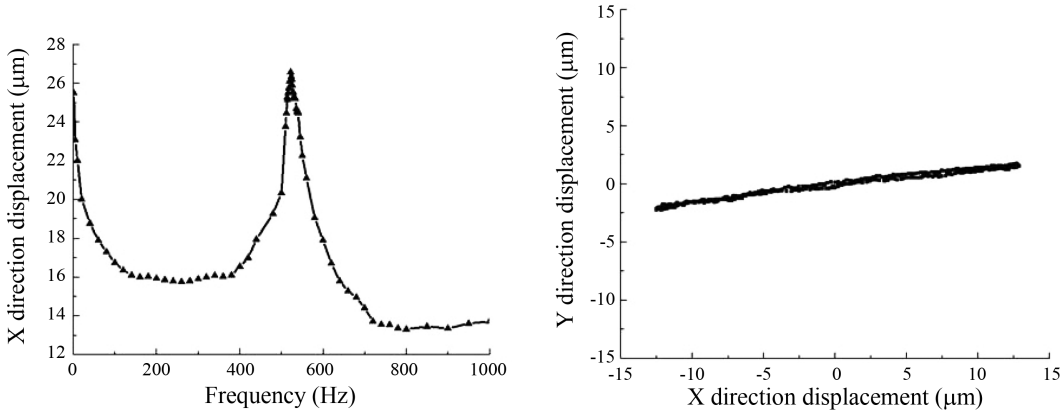

Fig. 12. (a) Displacements in X direction at different frequencies. (b) Output trajectory at 522 Hz.

displacement. A SQLab II vibration and noise test system is used to measure the vibration acceleration of the actuator. Fig. 10 shows the 3-D real-time vibration acceleration of the actuator (f = 500 Hz). The results show that the acceleration in X direction, Y direction and Z direction are 8 m/s^2, 9 m/s^2 and 0 m/s^2. The total acceleration is 12 m/s^2. According to the Newton's second law, the total output force is 0.36 N (the mass of the output head is 30 g). The maximum output force calculated by the theoretical model is 0.35 N (In Fig. 7). The theoretical results agree well with the experiment for the output force.

Resonance frequency is one of the important parameter to be measured for predicting the performance in high frequency applications. The six order natural frequency of the actuator are calculated by the finite element method, as shown in Fig. 11. They are 500.47 Hz, 500.62 Hz, 1185.7 Hz, 3318.5 Hz, 3319.6 Hz and 3812.5 Hz. We can find that the vibration mode of the first order mode is vibration in the Y direction, while the vibration direction of second order mode is in the X direction. Taking the pair of A and C rods working for example, the displacements of the Y direction and the X direction are measured, and the resonant frequency of the actuator is determined by experiments. Fig. 12a shows the output displacement of the output head from 1 Hz to 1000 Hz in X direction. It can be found that the output displacement is larger at low frequency (less than 50 Hz). Then, resonance occurs within the range 350 Hz-570 Hz. The response frequency is 522 Hz. Through experiments, it is found that the resonance frequency in the Y direction is also 522 Hz. The experimental results agree with the calculated one. The maximum output displacement in the X direction at 522 Hz can reach 27 μm. When the response frequency is found, the output trajectory of the actuator is measured, as shown in Fig. 12b. The output head is mainly vibrating in the X direction. The output trajectory is approximately straight. In addition, the hysteresis is very small when the actuator is operating at the resonant frequency. It can prove reliability and reproduce the designed actuator vibration process.

4. Conclusion

The 3-D micron-scale actuator is designed and fabricated. By controlling the magnetic field of the four rods, the actuator can produce 3-D controllable large output displacement and output force. The magnetic circuit of the actuator is analyzed, and the results show that the magnetic flux leakage is very little in the new structure. Based on the structural dynamic model, the theoretical model of output displacement and force of the actuator are established and calculated. An experimental platform is built and the experimental results of the output displacement and force are consistent with the theoretical analysis. The maximum X, Y and Z direction displacements are 46 μm, 46 μm and 8.2 μm, respectively. The total output force is 0.36 N. Moreover, the research can effectively investigate the effects of the frequency on the output displacement. The first two order resonant frequencies of the actuator are found to be 522 Hz in Y direction and X direction. The results show that the actuator not only realizes miniaturization, but also can output stable large output displacement and output force. The output head of designed actuator can achieve a variety of trajectories according to actual demands. The actuator can be used in precision machining systems.

Acknowledgements

This work was supported by the National Natural

Science Foundation of China (Grant No. 51777053), the Natural Science Foundation of Hebei Province (Grant No. E2016202034, and E2017202035).

References

[1] E. Brinksmeier, O. Riemer, and A. Gessenharter, Precis. Eng. **30**, 325 (2006).
[2] H. Suzuki, S. Kodera, T. Nakasuji, T. Ohta, and K. Syoji, Int. J. Jpn. S. Prec. Eng. **60**, 1280 (1997).
[3] J. B. Restorff, M. Wun-Fogle, E. Summers, R. Kaufman, and N. J. Jones, Smart Mater. Struct. (2018).
[4] V. Dabade, R. Venkatraman, and R. D. James, J. Nonlinear Sci. **29**, 415 (2019).
[5] Y. Li, B. Wang, W. Huang, L. Weng, and Y. Li, AIP Adv. **9**, 035238 (2019).
[6] G. Xue, P. Zhang, Z. He, B. Li, and C. Rong, Smart Mater. Struct. **26**, 05LT02 (2017).
[7] Z. Deng and M. J. Dapino, Smart Mater. Struct. (2017).
[8] G. Xue, P. Zhang, Z. He, D. Li, Y. Huang, and W. Xie, [J]. J. Magn. Magn. Mater. **420**, 185 (2016).
[9] Y. Xu and X. Shang, Mater. Res. Express (2019).
[10] Z. Wang, Y. Zhu, R. Li, C. Liu, and N. Bruno, J. Intel. Mat. Syst. Str., 1045389X19849247 (2019).
[11] Y. Li, W. Huang, B. Wang, X. Cui, R. Yan, and Z. Yang, ICEMS (2017).
[12] R. Sathish Kumar and K. Jayabal, J. Appl. Phy. **125**, 194101 (2019).
[13] T. Ueno, C. Saito, N. Imaizumi, and T. Higuchi, Sensor Actuat. A Phys. **154**, 92 (2009).
[14] J. Guo, H. Suzuki, and T. Higuchi, Precis. Eng. **37**, 81 (2013).
[15] T. Kosawada, T. Koizumi, K. Ugajin, Z. Feng, and K. Goto, Microsyst. Technol. **22**, 45 (2016).
[16] Z. Deng, M. J. Dapino, Smart Mater. Struct. **27**, 113001 (2018).
[17] Z. Li, X. Zhang, G. Y. Gu, X. Chen, and C. Y. Su, IEEE T. Ind. Inform. **12**, 980 (2016).
[18] J. Atulasimha, Ph.D Diss. Dep. Aer. Eng. Md. (2006).